Atomic scale high-angle annular dark field STEM analysis of the N configuration in dilute nitrides of GaAs

M. Herrera,[1,*] Q. M. Ramasse,[2] D. G. Morgan,[1] D. Gonzalez,[3] J. Pizarro,[4] A. Yáñez,[4] P. Galindo,[4] R. Garcia,[3] M.-H. Du,[5] S. B. Zhang,[6] M. Hopkinson,[7] and N. D. Browning[1,8]

[1]*Department of Chemical Engineering and Materials Science, University of California–Davis, Davis, California 95616, USA*
[2]*Lawrence Berkeley National Laboratory, 1 Cyclotron Road, Berkeley, California 94720, USA*
[3]*Depto. de Ciencia de los Materiales e I.M y Q.I., University of Cadiz, 11510 Puerto Real, Cadiz, Spain*
[4]*Depto. de Lenguajes y Sistemas Informáticos, University of Cadiz, 11510 Puerto Real, Cadiz, Spain*
[5]*Materials Science & Technology Division, Oak Ridge National Laboratory, Oak Ridge, Tennessee 37831, USA*
[6]*Department of Physics, Applied Physics and Astronomy, Rensselaer Polytechnic Institute, Troy, New York 12180, USA*
[7]*Department of Electronic and Electrical Engineering, University of Sheffield, Sheffield S1 3JD, United Kingdom*
[8]*Lawrence Livermore National Laboratory, 7000 East Avenue, Livermore, California 94550, USA*

(Received 20 May 2009; revised manuscript received 2 September 2009; published 30 September 2009)

While high-angle annular dark field scanning transmission electron microscopy (HAADF-STEM) has been successfully used for the analysis of heavy atoms in a lighter matrix, the detection of light atoms in a heavy matrix remains challenging. In this paper, we show that the combination of first-principles total-energy calculations with aberration-corrected HAADF-STEM experimental and simulated images can be used to overcome this problem. The application of this methodology to the analysis of dilute nitrides of GaAs points to the existence of a major proportion of $(2N_{As})_{nn}$ in the alloy, which is a relatively stable configuration in GaAsN as revealed by our energetic calculations. Our study has allowed us to shed light in the effect of the local distortion of the lattice due to different configuration of atoms in HAADF-STEM imaging.

DOI: 10.1103/PhysRevB.80.125211 PACS number(s): 68.37.Ma, 68.55.Ln, 68.65.Fg

I. INTRODUCTION

In the last decades there has been great interest in extending the possibilities for band-structure engineering in III–V-based materials by alloying with N. The addition of small quantities of N to III–V compounds produces a large band-gap bowing that gives place to a substantial extension of the emission wavelength range[1,2] allowing, for instance, operation at the transmission windows of optical fibers (1.55 μm) in GaAs related compounds. This unusual behavior is a consequence of the small size and high electronegativity of N that strongly modifies the conduction band, although nowadays there is an intense debate on the role of anticrossing[3] and cluster state models[4] to find a complete explanation for this behavior.[5] In any case, the accurate control of the photoluminescence emission wavelength can be only achieved by a careful control of the N content in the alloy and a perfect stabilization of the structure.[6] The inventory of the ternary and quaternary dilute-nitride alloys based on III–V compounds has been rising in the last decade exploring all the combination between III elements (Al, Ga, and In) and V elements (P, As, and Sb). Among them, the dilute nitrides of GaAs have logically been the first and the most scrutinized and they have shown properties not usual in conventional III–V.[7,8] In spite of this, many features are not well understood yet and the key reason for this is the lack of knowledge of how the nitrogen atoms are inserted into the zinc-blende structure of III–V compounds.

First, although the thermodynamic solubility of N in GaAs is extremely low (less than 10^{14} cm^{-3}),[9] GaAsN alloys with N content as high as 10% have been reported.[10] This anomalous behavior has been associated with specific surface reconstructions during the epitaxial growth[11] and the formation of alternative N complexes in the alloy.[12] Second, an instability of as-grown samples exists and the subsequent annealing treatments cause a severe degradation of the minority-carrier lifetimes.[13,14] The formation of point defects such as N-N split interstitial[15] and the As_{Ga} antisite[16] have been suggested as electron traps in the Ga(In)NAs alloy, and also clustering of N atoms has been reported to dominate the emission in dilute nitrides of GaAs,[17] creating energy levels below the conduction-band energy that get deeper as the number of N atoms increases.[18] The degradation of the structural quality of the alloy has been directly related to the initial configuration of N at atomic scale[19,20] and therefore its characterization is of primary interest to understand the electrical and optical properties and thus optimize the performance of this system.

Yet the direct observation of individual atoms and their neighborhood in a material remains challenging and it has been the subject of intensive effort over the last few decades, dating back to 1970s when Crewe *et al.*[21] first reported the observation of single atoms (U and Th) on a thin carbon film using scanning transmission electron microscopy (STEM). More recently, the development of aberration corrector lenses and the associated improvement in spatial resolution has allowed the high-angle annular dark field (HAADF-) STEM technique to be used to image single atoms in materials such as semiconductors and catalysts[22–24] and, in combination with electron-energy-loss spectroscopy (EELS), the identification of single La atoms inside $CaTiO_3$.[25] A shared characteristic of all these experiments, however, is the fact that they deal with the detection of heavy atoms on/in a lighter matrix, where the contrast due to these atoms is reasonably high and their detection feasible. However, there are no previous results for the detection of light atoms in a heavy

 ©2009 The American Physical Society

matrix (which is required for N in GaAs), where the relative change in contrast due to the light element is very small.

The reason for this lies in the basis of the technique. HAADF-STEM is an advanced microscopy technique that allows obtaining pure compositional information from a material by scanning an atomic scale focused probe over a zone-axis oriented crystals and collecting the high-angle scattering with an annular detector. As we become concerned with higher scattering angles, the coherent Bragg scattering is overtaken by thermal diffuse scattering (TDS), which is the main contribution to the image. TDS is directly related to the average Z number of the material and, in general, it has been considered that the HAADF signal is a function of Z^n where n ranges between 1.6 and 2.[26,27] According to this, a heavy atom can be evidenced inside of a lighter matrix but a light atom is tricky to detect in a heavy matrix. Thus, the possibility to detect a light atom in a heavier matrix should be related to other factors affecting HAADF imaging

In this sense, it should be highlighted that the static atomic displacements (SAD) associated to lattice defects in imperfect crystals could play a major role in HAADF-STEM imaging. Although these effect of SAD in the image intensity of HAADF-STEM micrographs was pointed out in early studies by Perovic *et al.*[28] and Treacy *et al.*,[29] only few papers have been published discussing this subject after that, and in general the effect of SAD in HAADF-STEM has not been analyzed and quantified in as much detail as needed to completely understand HAADF-STEM images of nonperfect crystals. In this sense, Grillo *et al.*[30] have recently published an exhaustive analysis of the effect of SAD due to the introduction of heavier In atoms in GaAs. Moreover, the effect of SAD has been brought up to explain the unexpected contrast reversal observed in B-doped Si quantum wells[28] as well as N containing GaAs wells,[31] although the differences in contrast due to different possible configuration of atoms around the N have been neglected.

The aim of this work is twofold. First, we have used a methodology based in the combination of first-principles total-energy calculations with aberration-corrected HAADF-STEM experimental and simulated images to shed light in the behavior of the smaller alloy constituent N in GaAs(N) quantum wells (QWs). The results of this analysis point to the existence of alternative N-related complexes beside substitutional N in the dilute nitrides of GaAs, which would have a strong effect in its optoelectronic properties. Second, this study has allowed us to investigate the effect of SAD in HAADF-STEM images for different configuration of atoms of the same nature, e.g., different substitutional and interstitial N complexes in GaAs, and for different N compositions. This study demonstrated the strong influence of the distribution of atoms in the intensity of HAADF-STEM images.

II. EXPERIMENTAL DETAILS

The studied GaAsN QWs were grown on a GaAs(001) substrate in a VG V80H molecular-beam epitaxy (MBE) system equipped with an Oxford Applied Research HD25 radio-frequency plasma source for N. The N composition was controlled by monitoring the optical intensity of the atomic N plasma emission. The sample consisted of four groups of three GaAsN quantum wells with a thickness of 8 nm sandwiched between GaAs barriers. Every group of wells was grown with a different composition in N: 0.1%, 0.4%, 1%, and 2.5%, and separated from the next group by AlAs markers. The sample was grown at 460 °C and no postgrowth thermal annealing was applied.

The sample was thinned to electron transparency in cross-section geometry using a standard sample preparation technique. After grinding, dimpling and polishing, a Fishione Ar^+ ion miller was used with a 3 kV beam at an 8° incident angle cooled by liquid N_2. After a hole was milled in the specimen, the surface of the sample was cleaned by milling at 1.5 kV during 20 min also cooled with liquid N_2.

The high-resolution HAADF-STEM study was performed using an aberration-corrected VGHB501 dedicated STEM operated at 100 kV with spatial resolution of the sub-angstrom level. A detector angular range of 72–210 mrad for a convergence angle of approximately 20 mrad was used: under these conditions, the contribution of Bragg diffraction effects to the image is minimal.[32] The low-resolution HAADF-STEM images were obtained in a JEOL 2500 (S)TEM, operated at 200 kV with a detector angular range of 55–143 mrad.

In this study, we are comparing the HAADF-STEM intensity obtained from different GaAsN wells. In order to be able to compare quantitatively the intensity of different HAADF-STEM images, attention should be paid to microscope- and sample-related parameters during the acquisition. For each microscope, the series of images used for the comparison were acquired under the same conditions of the lenses, exposure time, and brightness/contrast settings, which was possible given that all the wells are integrated in the same structure. Attention was paid to calibrate the black level of the images to obtain a true value for the image intensities[33] and also to avoid saturation of the intensity in any part of the images. With regard to the sample, the thickness of the foil under study is a determining factor affecting the contrast in a STEM micrograph.[34] Low-loss electron-energy-loss spectra using intensity ratios of the area under the zero-loss peak to that under the whole spectrum was used to measure the thickness of the TEM foil[35] for the different QWs. The thickness of the sample foil for the experimental study was chosen as 70 nm; while this is certainly thick for high-resolution TEM imaging standards, it provided an ideal compromise for this particular study: it is relatively thick to avoid surface stress relaxation contributions[36] but still thin enough so scattered intensity from the whole sample foil contributes to atomic structure images.[34]

Although rarely reported, the introduction of N dopants may also lead during the thinning procedure to different sputtering rates of the quantum wells and the GaAs substrate under the ion beam. The presence of any preferential drilling was therefore closely monitored by relative thickness measurements by EELS. Grooves at the interfaces between the substrate and the doped wells were indeed observed on occasion and the N-rich wells were measured to be around 3% thicker on average than the undoped GaAs, irrespective of the N concentration. The intrinsic uncertainty in this method is relatively high,[38] up to 10–20 %:[37,38] the recorded values

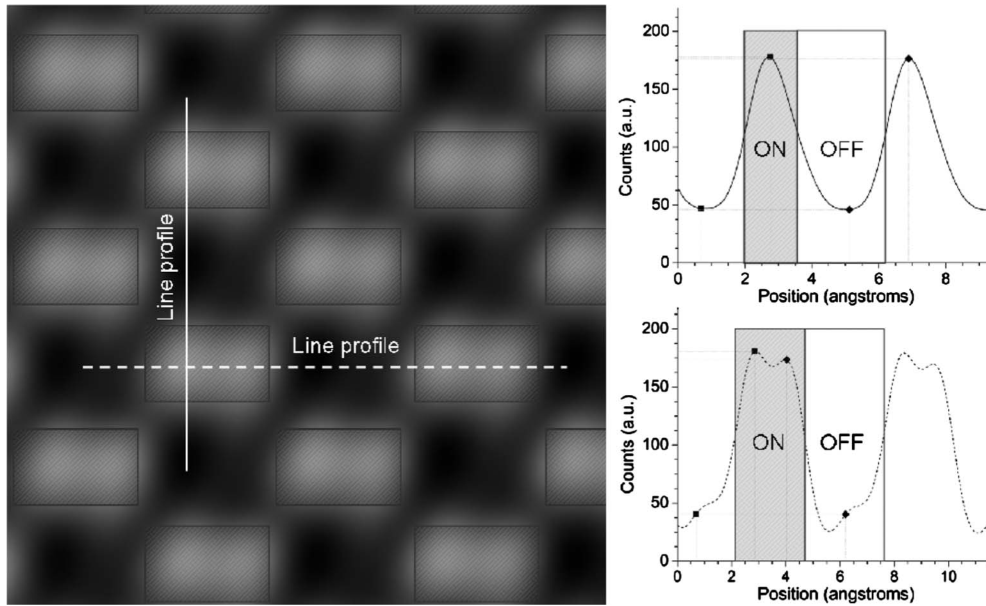

FIG. 1. Definition of the on the atomic columns and valley between the atomic columns areas in the averaged patches (patch from a 1%N well shown here). Line profiles are used to define the "on the column" boxes, as symbolized left; the complement image defines the off the column intensity.

were nevertheless taken as indicative of the general trend and these thickness variations were taken into account when comparing experimental results with simulations.

The signal differences involved in this study are minute: a careful and systematic processing was applied to the high-resolution micrographs in order to measure the relative intensity on the atomic columns and the space between columns as a function of N content. Up to six and no fewer than three images were included for each of the four N concentrations. In order to avoid possible contamination buildup and minimize beam damage, only one image was recorded for each well, moving over to the next well in the sets of three available at every N concentration. Due to the high magnification necessary to retain a good enough visibility of the dumbbells, the entire well could not be included in one single frame. Care was therefore taken to include images from both the right- and left-hand sides of the well, thus taking into account any remaining contrast or thickness disparity across a single well.

Patches were cut out from the images of the GaAsN wells and the GaAs barrier, cross correlated across those regions and averaged; the areas close to the well boundaries, which may exhibit some interface grooving and subsequent intensity artifacts as sometimes observed in the experimental thickness profiles, were excluded from the cross correlations. These averaged patches were then analyzed to generate the intensity data points from the atomic columns and from the valleys between the columns. For consistency, the areas denoted by "on the atomic columns" or "valley between the columns" were systematically defined as follows: line profiles were taken across the atomic columns, with a line width corresponding to the estimated microscope point spread function. These profiles were used to select a box around the dumbbells for which the intensity lay above the half point between the peaks and average background value. The set of all such boxes was defined as on the atomic columns, and the complement region was defined as valley between the columns, as shown in Fig. 1.

The probe profile calculations were based on the aberration coefficients measured before recording the series of images and yielded an estimated full width half maximum of the probe of 1.082 Å, for a corresponding 59% intensity radius $d_{59}=1.396$ Å.[39] The errors shown in the plot correspond to the standard error of the mean when taking the average over the various images.

HAADF-STEM image simulations were carried out considering different substitutional and interstitial N-containing complexes, and with the experimental parameters of the VGHB501 microscope. The equilibrium lattice positions of the atoms in fully relaxed GaAsN complexes used as input in the simulations as well as the energy of these complexes were calculated using density-functional theory (DFT) within the local-density approximation, as implemented in Vienna *ab initio* simulation package.[40] For this, the electron-ion interactions were described by projector-augmented wave pseudopotentials.[41] The valence wave functions were expanded in a plane-wave basis with cutoff energy of 400 eV. All the calculations were performed using 64-atom cubic cells. A $2\times2\times2$ grid was used for the k-point sampling of Brillouin zone. All the atoms were relaxed to minimize the Feynman-Hellmann forces to below 0.02 eV/Å. The defect formation energy is defined as:

$$\Delta H_f = \Delta E - \sum_i n_i(\mu_i + \mu_i^{ref}) + q(\varepsilon_{\mathrm{VBM}} + \varepsilon_f), \quad (1)$$

where ΔE is the energy difference between the defect-containing and defect-free supercells, and n_i is the difference in the number of atoms for the ith atomic species between the defect-containing and defect-free supercells. μ_i is a rela-

tive chemical potential for the ith atomic species referenced to μ_i^{ref}. For Ga and As, μ_{Ga}^{ref} and μ_{As}^{ref} are the chemical potentials for bulk Ga and bulk As, respectively. For N, μ_N^{ref} is taken as half of the energy for an isolated N_2 molecule. The q parameter in Eq. (1) is the defect charge state and ε_f is the Fermi energy referenced to the valence-band maximum (VBM), ε_{VBM}. For the calculation of the energy of the complexes, we have set $\mu_N=0$, according to the N-rich conditions of the growth process.

HAADF-STEM images were computed using the simulation software SICSTEM, fully described in Ref. 42. Elastic scattering was implemented following Kirkland's approach, while TDS was included using a local TDS absorptive potential approach, according to Refs. 43 and 44. Simulation results have been successfully compared to Ishizuka's fast Fourier transform multislice approach theoretical results and to STEM for WINHREM™ software. Due to the high computational requirements needed in analysis such as the one described in this paper, the software runs in 256-parallel xenon cluster, allowing an improvement of approximately 350 times in processing time when compared to a single-node machine.

The N atoms were located in random positions in three dimensions in the simulated structure and the same image processing treatment as in the experimental images was applied in order to average the contrast along the images, separately for the atomic columns and for the space between the columns. The thickness of the simulated structures was chosen in agreement to the experimental ones. In order to simulate different compositions in the supercell, the following procedure was applied. First, a pure GaAs $10\times10\times70$ nm supercell was generated. Then an As atom in the supercell was randomly chosen. The As atom in the supercell was substituted by a N atom, modifying as well the atom positions around it according to the DFT cell. Following this procedure iteratively, different numbers of DFT cell were added depending on the N concentration. Twenty different supercells with around 4000 atoms were generated from five different DFT cells (substitutional and interstitial N) and four different N ratios: 0.5%, 1%, 1.5%, and 2%. For each DFT cell-composition pair, different thickness supercells were built (1.25, 7.5, 13.75, 20.0, 26.25, 32.5, 38.75, 45.0, 51.25, 57.5, 63.75, and 70.0 nm).

The whole images were simulated in each case to reduce the error in the measurement since at low concentration the N content is not the same in each atomic column. In a random distribution of N, the intensity profiles vary among the dumbbells since they depend not only on the number of N atoms inside the atomic column but even on their position on the column (in the beginning or in the end of the electron path reducing the top bottom effect) and the atomic neighborhood. The simulation of square areas that includes up to ten dumbbells allowed us to obtain a more realistic average of both peak and valley intensities similar to the experimental ones.

The dumbbell spacing has been also measured from simulated and experimental images in order to obtain information on the strain state of the wells. Provided the appropriate statistical and image-processing precautions are taken, it has been shown that lattice spacings measured from aberration-corrected HAADF images could be used to quantify strain.[45] Lines profiles were taken across the each of the experimental and simulated dumbbells with a linewidth corresponding to the estimated microscope point spread function. The profile was then fitted through a nonlinear least-squares algorithm to a double Gaussian curve: the distance between the centers of the two Gaussians was taken as a measure of the ⟨004⟩ "dumbbell" spacing.

As we are dealing with relatively small differences in contrast/dumbbell spacing for the experimental and simulated images, we have performed a statistical analysis of the data to confirm that the differences found are significant so we can extract information from them. Initially, for each group of measurements we have computed the mean, the standard deviation and the standard error. Then, the analysis of variance by the one-way ANOVA procedure has been carried out, where an overall-ANOVA parameter less than 0.05 implies that at least two or more populations have statistical different means. Since the ANOVA test assumes that all the samples are drawn from normally distributed populations with equal variance, the Levene test was used to compare the variance of the data. After this, the Bonferroni posthoc means comparison was used to determine the number of pairs of data groups that show significant differences between them. As some of the data do not completely fulfill the requirements of the ANOVA test (which is reasonable due to the low N concentrations used, where there are atomic columns with N and others without it), a Kruskal-Wallis ANOVA (KWANOVA) test was also performed since it does not require the normal distribution of the population and it places less restriction on the comparison. In all the cases, we set the significance level as 0.05.

III. HAADF EXPERIMENTAL RESULTS

Figure 2(a) shows a low magnification HAADF image of the $GaAsN_{0.025}$ QWs where, as it can be observed, the wells appear brighter than the GaAs barrier. As mentioned before, the intensity in HAADF-STEM imaging of perfect crystals is considered proportional to Z^n.[26,27] The substitutional change in As($Z=33$) by N($Z=7$) leads to a reduced average atomic number of the well in comparison to the barrier and consequently, a reduced intensity would be expected when considering strictly the Z number rule. HAADF-STEM images of the wells with lower N composition also showed higher intensity than the GaAs barrier, as shown in Fig. 2(b) for 0.1%N and, as it can be observed, the contrast is decreased with the reduction in N composition. Figure 2(c) shows a plot of the contrast $GaAs_{1-x}N_x$-GaAs $[C=(I_{GaAsN}\text{-}I_{GaAs})/I_{GaAs}]$ vs %N (x). As we can see, the evolution of contrast with the N content does not follow a linear behavior: the slope of the curve for low N concentration is relatively large and for the higher N content the curve levels off. Though the origin of this anomalous contrast may rely on the local distortion of the lattice due to the introduction of N, this behavior is not immediately clear for what is supposed to be a random substitutional alloy.

To investigate the origin of the observed evolution of contrast with %N, the QWs were analyzed by high-resolution

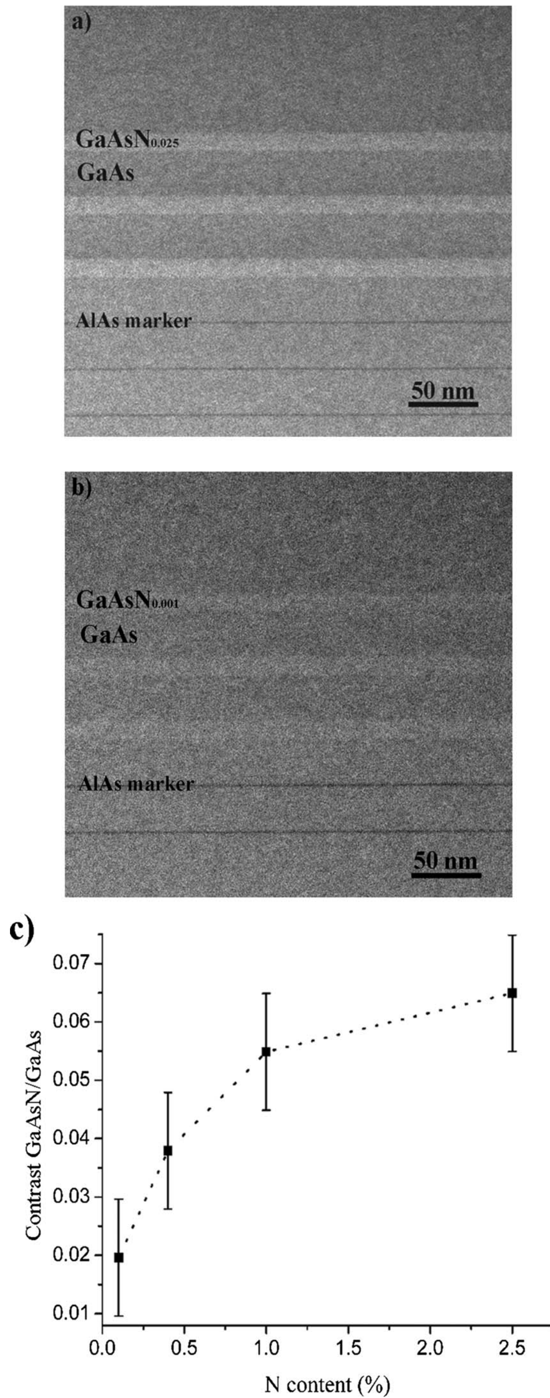

FIG. 2. Low magnification images of the samples with (a) 2.5%N and (b) 0.1%N; (c) plot of the evolution of contrast $(I_{GaAsN}\text{-}I_{GaAs})/(I_{GaAs})$ vs N content from the low magnification images of the GaAsN QWs.

HAADF-STEM with aberration corrector, as can be observed in Fig. 3 for 2.5%N. A detailed analysis of these images led us to a remarkable result. We have measured, separately, the contrast from the valley between the atomic columns and from the atomic columns themselves, and plotted it vs %N in Figs. 4(a) and 4(b), respectively. In order to assess whether the contrast for the different N compositions found in our analysis shows significant differences, the

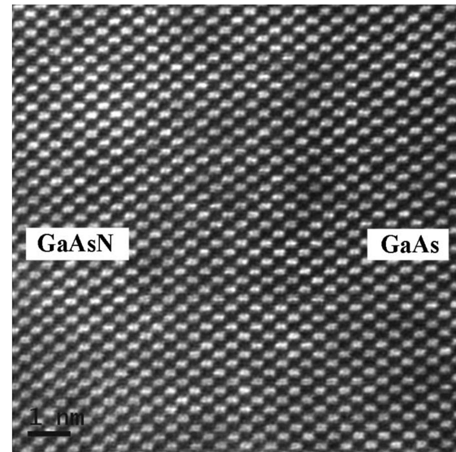

FIG. 3. High-resolution HAADF-STEM image of a QW with 2.5%N.

ANOVA test was applied. This test has shown that the contrast from the valleys for the different N contents are meaningfully different at the 0.05 level (overall ANOVA=4.85×10^{-5}) whereas the differences in contrast from the peaks are not significant (overall ANOVA=0.128).

As it can be observed in Fig. 4(a), the evolution of the contrast from the valley between the atomic columns shows a strong increase for the lower N compositions and then flattens off for higher N contents, similar to the behavior obtained from the low magnification images. (It should be noted that although the evolution of contrast is similar for the low- and high-resolution images, the absolute values are inevitably different given that they have been obtained with different microscopes under different conditions). However, the increase in contrast from the atomic columns is negligible as the statistical analysis has shown. The comparison between these curves reveals that the increased intensity found in GaAsN originates specifically from the valleys between the atomic columns rather than from the columns themselves, dominating the contrast from the well. This is in contrast to the results reported for the system SiGe/Si, where an increase in contrast from both the atomic columns and the background was observed.[46] This peculiar behavior points at an intrinsic characteristic of the lattice as the origin of the observed contrast, given that artifacts as those related to changes in thickness of the sample would give place to an increased intensity of both atomic columns and the space between them.[34]

Additionally, we have measured (also from individual dumbbells) the average dumbbell spacing ratio (referred to the GaAs dumbbell spacing) from the images and plotted vs N content in Fig. 4(c). The analysis with the ANOVA test showed that there are significant differences between these measurement (overall ANOVA=2.55×10^{-4} and KWANOVA=7.85×10^{-8}). As it can be observed in Fig. 4(c), the evolution of the dumbbell spacing with N content shows a nonlinear reduction when increasing the N content. This behavior is likely caused by the introduction of an additional strain component due to the incorporation of N in the lattice. However, different N configurations have been proposed for dilute nitrides of GaAs and its effect on the

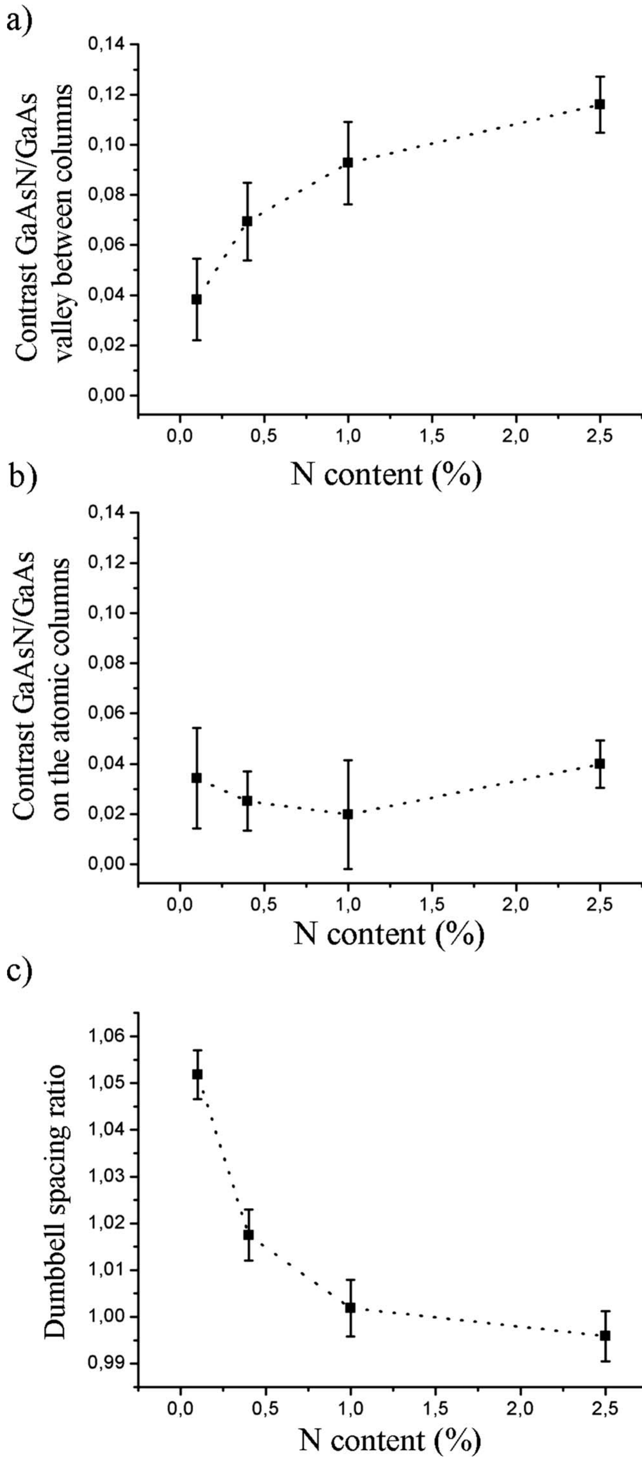

FIG. 4. Plot of the contrast measured from the high-resolution images (a) from the valley between the atomic columns and (b) from the atomic columns vs N content; (c) plot of the experimental average dumbbell spacing ratio *vs*. N content obtained from the high-resolution images.

local distortion is likely to be different. Our hypothesis is that the differences in the HAADF image parameters will allow elucidation of the predominant N configuration in the alloy using for this the comparison between experimental and simulated images.

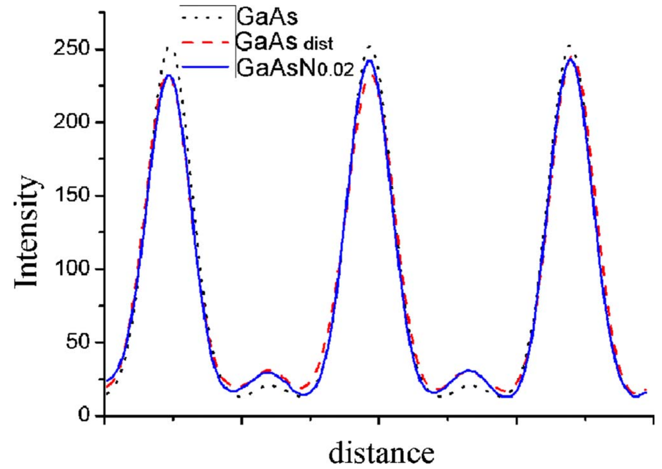

FIG. 5. (Color online) Line profiles taken from simulated images of pure GaAs (dotted line), GaAs with a lattice distortion similar to GaAsN (dashed line), and relaxed $GaAsN_{0.02}$ (solid line).

IV. HAADF SIMULATIONS

In order to explain the origin of the obtained results, simulations of the HAADF-STEM images for different N configurations in GaAsN were performed. As mentioned before, first-principles total-energy calculations were used to determine the equilibrium lattice positions of the atoms in fully relaxed GaAsN cells. These lattice sites where used as the input for the HAADF-STEM simulations. It is worth highlighting that care should be taken in the comparison of the absolute values of intensity in HAADF-STEM images obtained experimentally and from simulations, given that with the current codes used for the simulations this comparison may not be straightforward. A mismatch of 2–4 times between TEM (Ref. 47) or STEM (Ref. 34) images and simulations has been usually reported and the contribution of a nonexpected background in experimental HAADF-STEM images has been observed to increase monotonically with thickness and to reflect the Z number of the crystal.[34] This huge contrast mismatch (known as Stobbs factor) has been associated to an overestimation of the degree of coherence in the electron source, measured recently for zero-loss peak, plasmon loss and phonon-loss electrons as 0.3.[48] Our analysis through this paper will be based in the evolution of contrast with composition, not aiming to compare absolute values of intensity, so this contrast mismatch in not expected to alter our results significantly.

To begin with, we will consider the substitutional case, where N is located in the As lattice position. In general, this is the target in the successful growth of ternary or quaternary alloys with optoelectronic properties.

A. Substitutional case: The SAD effect

Figure 5 shows line profiles taken from simulated images of substitutional $GaAsN_{0.02}$ and pure GaAs structures in an equivalent position of the structure. As it can be observed, the profile corresponding to GaAsN shows an increased intensity in the valley between columns in comparison to GaAs (in good agreement with the experimental observations),

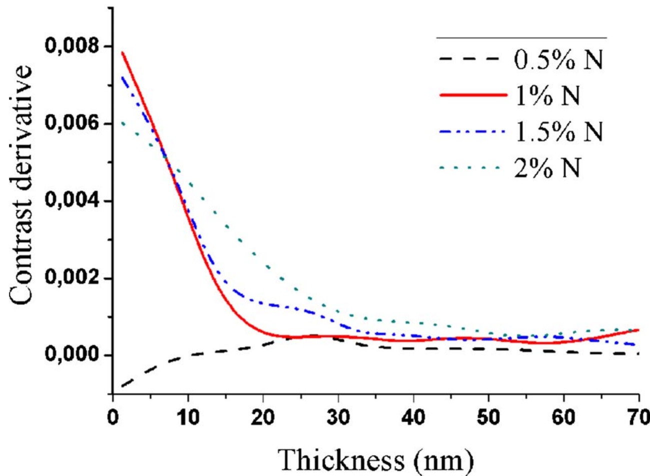

FIG. 6. (Color online) Plot of the contrast from simulated images of substitutional N with different N content vs specimen thickness.

whereas for GaAsN the intensity in the peaks varies depending on the atomic column, given that the distortion is different for each column. In order to separate the effect of the Z number from that due to the deformation of the structure, the simulation of a GaAs cell mimicking the local distortion of substitutional N was performed, where the N atom of a relaxed GaAsN structure was substituted by As without changing the position of the surrounding atoms. A line profile from this structure is also included in Fig. 5. As it can be observed, the simulation of such a structure also exhibited an increased intensity coming from the valley between columns, in the same way as in the substitutional N GaAsN structure, evidence that the intensity observed experimentally is basically due to the distortion of the lattice. This result shows the strong effect that the static atomic displacements can induce in HAADF-STEM images. This distortion of the lattice has an effect similar to the increase in lattice vibrations, enhancing the effective Debye-Waller factor of the host lattice[49] and, in some cases as shown in the present work, it can dominate over the Rutherford-scattering component. It should be underlined that the origin of this strain contrast is completely different to that typical in bright field (S-)TEM or low-angle ADF-STEM, where the contrast in the image depends on Bragg scattering effects and it is therefore coherent imaging. In the present study, we are using large detector inner angles (72 mrad) so the image is incoherent and the observed strain contrast stems from an increase in TDS due to the local displacement of the atoms.

It has been widely reported that the thickness of the sample is a parameter with a major effect in the intensity of HAADF-STEM images.[34] In order to analyze possible thickness-related artifacts in our study, the evolution of intensity with this parameter was computed. Figure 6 shows a plot of the contrast variations with the thickness, $\frac{\Delta C}{\Delta t}$, in GaAsN vs sample thickness up to 70 nm for the four N contents. As it can be observed, the contrast variations due to thickness variations are important for thicknesses below 30–40 nm but all the composition trends to a very small value for higher thicknesses. This means that the error in the

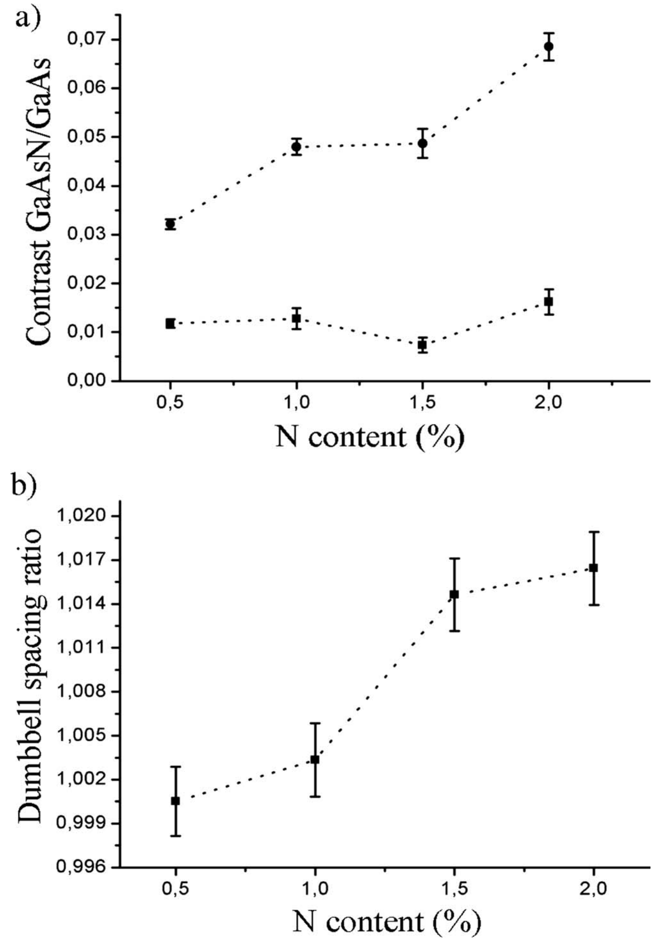

FIG. 7. (a) Plot of the contrast from the valley between columns (circles) and from the atomic columns (squares) and (b) dumbbell spacing ratio vs N content measured from the simulated images of GaAsN with substitutional N.

measurement of the thickness by EELS is not likely the origin of the increase in contrast found in our experiment.

Figure 7(a) shows a plot of the contrast GaAsN-GaAs from the simulated images computed with the substitutional N complex vs %N and Fig. 7(b) shows the evolution of the dumbbell spacing ratio obtained from the same image. Both the intensity and the dumbbell spacings were measured following the same procedure as in the experimental images. The ANOVA test showed significant differences for the dumbbell spacing ratio as well as for the contrast from the peaks and the valleys, although in the case of the peaks only one of the pairs of data showed significant differences in Bonferroni test vs the five pairs of data for the valleys. As we can observe, the contrast GaAsN-GaAs from the valleys shows an increasing slope for higher N contents. If we compare this evolution of contrast with the experimental result shown in Fig. 4(a), we can observe that there is a disagreement between them, given that the experimental study showed saturation for increasing N content. On the other hand, the dumbbell spacing ratio also follows the opposite tendency regarding the experimental study: in the experimental one the dumbbell spacing is reduced while for the simulation of substitutional N it increases with %N. This

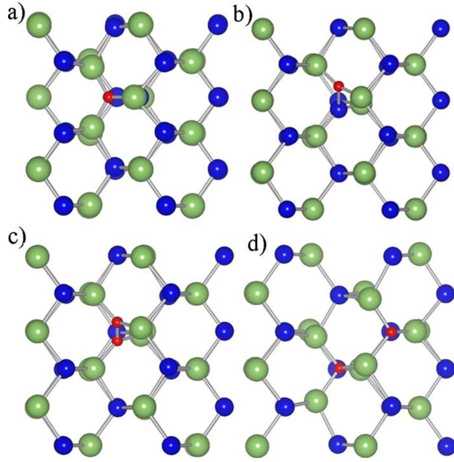

FIG. 8. (Color online) Schematic of the different N configurations considered in the present work: (a) $(As_{Ga}\text{-}N_{As})_{nn}$, (b) N-As split interstitial, (c) N-N split interstitial, and (d) $(2N_{As})_{nn}$ cluster. The small dark balls (red) represent N, the big light ones (green) are Ga, and the big dark ones (blue) are As.

different behavior suggests that we should consider the existence of alternative N configurations in the alloy besides random substitutional N.

B. Other nitrogen configurations

In the literature, the existence of several N configurations in GaAsN has been proposed. Thus, the existence of N-N split interstitials, N-As split interstitials or $(As_{Ga}\text{-}N_{As})_{nn}$ pairs in GaAsN has been suggested both theoretically[11] and experimentally.[50,51] Also, the low solubility of N in GaAs (Ref. 9) has been reported to induce the clustering of N atoms[52] in the alloy, although generally no specific configurations are proposed. Both interstitial N and N clustering could produce a change in the TDS from the GaAsN region. According to this, we have performed the simulation of GaAsN structures where N is incorporated in the group-V lattice sites (substitutional N) both randomly and in incipient clusters, and as interstitial configurations. Figure 8 shows a schematic of the different N configurations considered in the present work: (a) the $(As_{Ga}\text{-}N_{As})_{nn}$ pair, where nn stands for nearest neighbor; (b) N-As split interstitial, which would introduce a higher strain energy than the analogous with only N due to the larger size of As atoms, (c) N-N split interstitial, where the exceptionally strong N-N bond should be highlighted; (d) $(2N_{As})_{nn}$ cluster, precursor of a phase separation in the alloy.

Figures 9(a) and 9(b) plot the GaAsN-GaAs contrast from the atomic columns and the valleys between columns, and the dumbbell spacing ratio, respectively, measured from the simulated images of the complexes (a)–(c) in Fig. 8 following the same procedure as before. This plot shows that for each complex, the intensity from the valley between the atomic columns is higher than from the columns themselves due to the strong local distortion, as observed in the substitutional structure. Analyses of the variance of the measurements were performed to examine whether there are signifi-

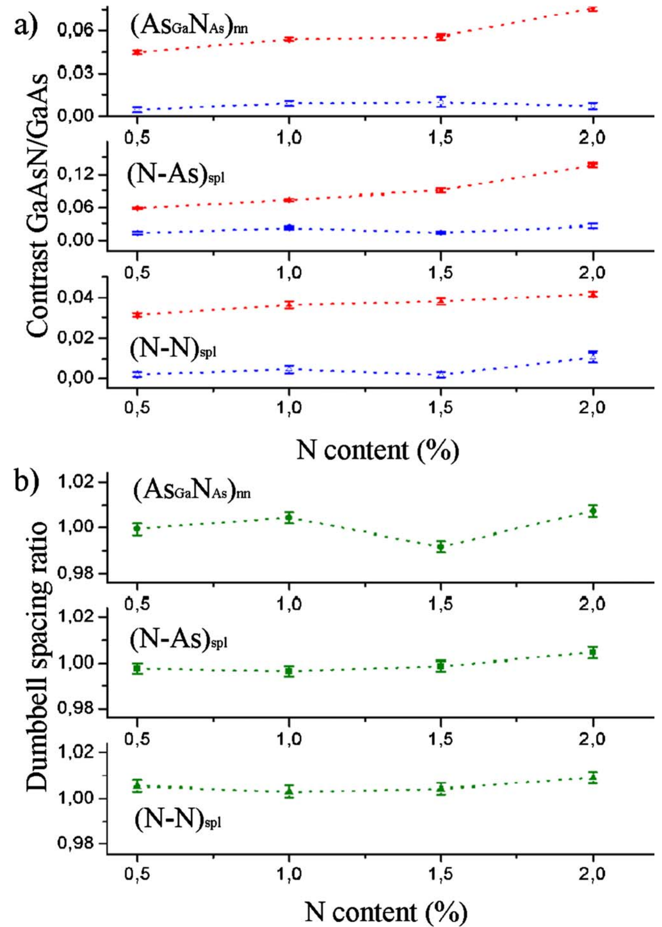

FIG. 9. (Color online) (a) Plot of the contrast from the valley between columns (closed symbols) and from the atomic columns (open symbols) and (b) dumbbell spacing ratio vs N content measured from the simulated images of GaAsN with the different complexes $(As_{Ga}\text{-}N_{As})_{nn}$, $(N\text{-}As)_{spl}$y$(N\text{-}N)_{spl}$.

cant differences for the studied N contents. The results of these tests reflect that in all cases the contrast from the valleys for the different N contents are significantly different at the 0.05 level. With regard to the peaks, even though some complexes pass the overall-ANOVA test, the Bonferroni test showed that there are only significant differences between at most one or two pairs of means, in contrast to the five-six pairs obtained for most of the valleys. Similar conclusions are obtained for the dumbbell spacings.

According to Fig. 9, the N-As split interstitial and the $(As_{Ga}\text{-}N_{As})_{nn}$ pair show an increase in the slope of the contrast from the valleys for higher N compositions, whereas the experimental results showed a reduction in the slope for this range. Moreover, the trend of the dumbbell spacing ratio with N content is to increase in all the configurations and they do not agree with the experimental observations. Consequently the existence of these complexes in the GaAsN alloy cannot explain the experimental results. For the N-N split interstitial, both the GaAsN-GaAs contrast and the dumbbell spacing ratio stays very stable with increasing N content. In this complex, an As atom (atomic radius $=1.2 \times 10^{-14}$ m) is replaced by two N atoms (atomic radius $=0.7 \times 10^{-14}$ m), therefore the local distortion is much

smaller than in the case of N-As split interstitial (strong compressive strain) or substitutional N (strong tensile strain), which justifies the small variations in contrast/dumbbell spacing with N composition for this complex and the absence of significant differences in the dumbbell spacing ratio found in the statistical analysis. According to these results, the formation of N-N split interstitials in GaAsN is not able to produce the strong bright contrast observed in our experimental HAADF-STEM images.

C. Cluster case

Up to now, we have simulated structures with N configurations distributed randomly in the GaAs supercell. The hypothesis of the nonproximity between complexes stems from the repulsive interaction between stresses of the same sign. However, the high interaction parameter of GaAs-GaN (2.16×10^5 J/mol) gives rise to a solid phase miscibility gap that would justify a trend of nitrogen to separate into a secondary GaN phase. The configuration of atoms in these initial stages of N clustering is not obvious. In this work, we propose a configuration formed by two close substitutional N [in the following called $(2N_{As})_{nn}$ cluster, see Fig. 8(d)], precursor of the phase separation into N-rich and N-poor regions. First-principles total-energy calculations were also used in this case to assess the equilibrium lattice positions of a fully relaxed cell containing this complex, which were used for the image simulations.

Figure 10 shows the plot of the contrast GaAsN-GaAs from the atomic columns and from the valleys between columns, and the dumbbell spacing ratio, corresponding to the simulated images of the $(2N_{As})_{nn}$ cluster. The statistical analysis showed significant dissimilarities for the contrast from the valleys and from the peaks with the N content, as well as for the dumbbell spacing ratio. As we can observe, this complex is the only one for which the evolution of contrast with composition shows the same tendency as found in the experimental micrographs, an increase in contrast with a reduction in the slope for higher N contents. Moreover, the evolution of the dumbbell spacing ratio for this complex is also the only one where simulations and experimental images coincide, decreasing for higher N contents with the same tendency. Thus, this dumbbell spacing ratio is reduced for increasing %N with a slope very similar to the experimental images in every computed composition step, as can be seen from the comparison of the Figs. 4 and 10 (the slope is −0.011 and −0.00247 in the simulation vs −0.017 and −0.00223 in the experimental analysis for the intervals 0.5−1 %N and 1−2 %N, respectively). This result shows that the preferential formation of this complex in the alloy over the interstitial configurations would explain our experimental results by HAADF-STEM. In line with this, substitutional N pairing up to four neighbor position in $GaAs_{1-x}N_x$ alloys with concentrations of $x<0.025$ has been reported previously,[53] in accordance with our experimental finding.

Even though we have obtained that the HAADF results could be explained by the SAD effect from the $(2N_{As})_{nn}$ cluster, we should keep in mind that the existence of this or other N configurations in the alloy strongly depend on the thermodynamic stability of such configurations. Because of this, in the following we will analyze the formation energy of the different complexes considered in the present work.

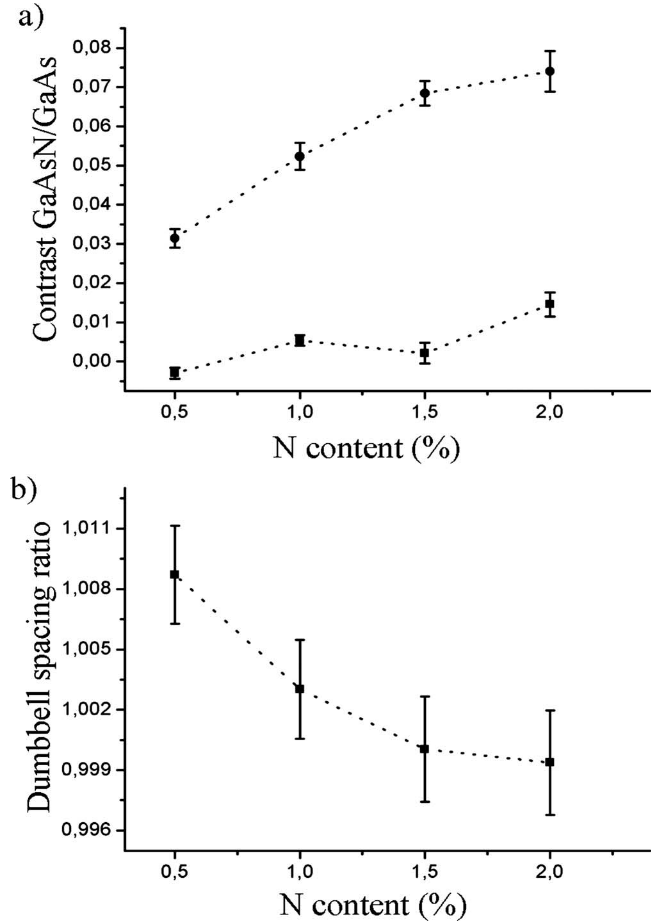

FIG. 10. (a) Plot of the contrast from the valley between columns (circles) and from the atomic columns (squares) and (b) dumbbell spacing ratio vs N content measured from the simulated images of GaAsN with the $(2N_{As})_{nn}$ cluster.

V. DEFECT FORMATION ENERGY

Figure 11 shows a plot of the energy of the different complexes considered in this work vs As chemical potential (μ_{As}) obtained from first-principles calculations as explained in Sec. II. As we can observe, the higher energy corresponds to the interstitial complexes, mainly to $(N\text{-}As)_{spl}$ and $(As_{Ga}\text{-}N_{As})_{nn}$, which would then be the more unlikely configurations in the alloy. This coincides with our simulation study where the plots of contrast/dumbbell spacing for these two configurations differ the most from the experimental results. On the other hand, substitutional N and $(2N_{As})_{nn}$ are the configurations of lower energy and thus more stable, being $(N\text{-}N)_{spl}$ located in an intermediate position. Our microscopy results have shown that $(2N_{As})_{nn}$ is the configuration where there is a better agreement of the evolution of contrast and dumbbell spacing ratio between experimental and simulated images. However, slight differences in the slope of the curves have been observed, being reduced in $(2N_{As})_{nn}$ with

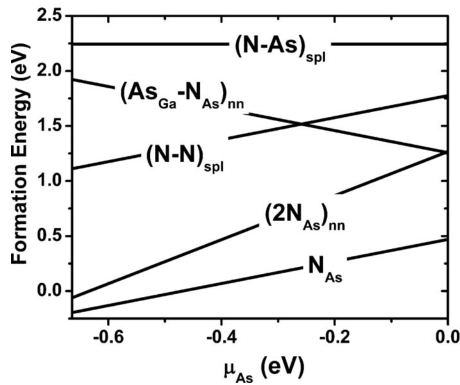

FIG. 11. Formation energy of the different complexes calculated with the density-functional theory within the local-density approximation vs As chemical potential (μ_{As}).

regard to the experimental observations. This could be due to the probable existence of a mixture of different types of complexes in the alloy, where $(2N_{As})_{nn}$ would be majority thus defining the main shape of the plots. Care should be taken when considering the contrast corresponding to a structure with a mixture of N complexes as equivalent to the sum of the contrast associated to independent structures each one with only one type of complex, given that this sum may not be so straightforward due to a possible different behavior of the electron beam when finding a different configuration of atoms. However, qualitative general tendencies can be inferred from the plots of the independent complexes. According to Fig. 9, the increase in contrast/dumbbell spacing due to the existence of $(N\text{-}N)_{spl}$ in the alloy is very small, therefore a mixture of $(2N_{As})_{nn}$ with $(N\text{-}N)_{spl}$ would produce a reduction in the slope of the contrast with regard to pure $(2N_{As})_{nn}$, contrary to our experimental results. Thus the existence of a big amount of this complex would not agree with our experimental observations despite its relatively small associated energy. On the other hand and as shown in Fig. 11, substitutional N is the complex of smallest energy, which makes it a good candidate to be present in the alloy. The existence of substitutional N would not change much the contrast corresponding to the higher N composition [where the bigger difference in slope between experimental results and $(2N_{As})_{nn}$ is] given that the obtained value is pretty similar to that corresponding to $(2N_{As})_{nn}$, and the dumbbell spacing ratio follows the opposite tendency as in the experimental study, so at the sight of these results it is difficult to estimate the proportion of this complex in the alloy. In order to obtain a higher relative intensity for the higher N content as observed experimentally, the existence of N-As split interstitial is a possibility given that it shows the highest contrast found in our study. However and as mentioned before, the huge energy associated to this complex makes the existence of a large proportion of this configuration in the alloy unlikely.

The explanation of the predominance of N dimmer complexes must be looked for in the methods to supply active nitrogen species used for the growth of III-nitrides by MBE. Radio-frequency nitrogen plasma sources are commonly used for the growth of III-nitrides by plasma-assisted MBE. Their output mainly consists of a mixture of atomic nitrogen as well as metastable excited molecules.[54,55] It has been widely reported that the excited nitrogen metastable molecules are the species predominantly responsible for the growth of III-nitrides.[56] The incorporation of the N cluster atoms may then occur on the surface of the structure during the epitaxial growth by MBE. These N clusters may be frozen into the lattice as the growth proceeds because the relatively low growth temperature ($\sim$460 °C) does not allow thermal equilibration. A different kinetic effect (involving hydrogen) has also been invoked previously to explain the similar N clustering in GaAsN grown by gas source MBE.[57] The primary driving force for the N clustering could be the low equilibrium solubility of N in GaAs.[9] N can be incorporated substitutionally into epitaxially grown MBE films thanks to the use of highly nonequilibrium growth conditions but yet the tendency to form a secondary NN cluster[9] can never be completely suppressed. Proof of this is the observation of Ga depleted Ga(In)As areas with walls of a GaN-like composition in Ga(In)NAs films with high N contents ($\sim$10%N).[52] The $(N\text{-}N)_{spl}$ cluster could evolve spontaneously to the $(2N_{As})_{nn}$ configuration during the growth or even the postannealing treatments due to the huge difference on the formation energy between the complexes. Further work is in progress to asses the weight of the $(2N_{As})_{nn}$ configuration in the total N content in GaAsN nitride dilutes alloys.

VI. SUMMARY

In summary, we have developed a complex methodology involving aberration-corrected HAADF imaging and simulations, first-principles calculations of different N complexes and the statistical analysis of the results for the challenging study of low *Z* number dopants in a heavy matrix. This methodology has been applied to a complex but technologically relevant system, namely, the dilute nitrides of GaAs. We have found that the existence of a major proportion of $(2N_{As})_{nn}$ in the alloy, which is a relatively stable configuration in GaAsN as our calculations have revealed, could explain our experimental results by HAADF-STEM, although a mixture of this complex with some other N configurations is obviously expected. Our study has allowed us to investigate the effect of the local distortion of the lattice due to different configuration of atoms in the intensity of HAADF-STEM images, which has evidenced the importance of SAD is the correct interpretation of HAADF-STEM images.

ACKNOWLEDGMENTS

This work was supported in part by a grant from the European Union under Contract No. MOIF-CF-2006-21423, Spanish CICYT Project No. MAT2007-60643, DOE under Grant No. DE-FG02-03ER46057, U.S. Department of Energy under Contract No. DE-AC02-05CH11231, and DOE Office of Nonproliferation Research and Development NA22.

*Corresponding author. Present address: Dep. de Ciencia de los Materiales e I.M y Q.I., University of Cadiz, 11510 Puerto Real, Cadiz, Spain.

[1] M. Kondow, K. Uomi, A. Niwa, T. Kitatani, S. Watahiki, and Y. Yazawa, Jpn. J. Appl. Phys. **35**, 1273 (1996).
[2] Su-Huai Wei and Alex Zunger, Phys. Rev. Lett. **76**, 664 (1996).
[3] W. Shan, W. Walukiewicz, J. W. Ager III, E. E. Haller, J. F. Geisz, D. J. Friedman, J. M. Olson, and S. R. Kurtz, Phys. Rev. Lett. **82**, 1221 (1999).
[4] P. R. C. Kent, L. Bellaiche, and Alex Zunger, Semicond. Sci. Technol. **17**, 851 (2002).
[5] A. Lindsay and E. P. O'Reilly, Phys. Rev. Lett. **93**, 196402 (2004).
[6] R. S. Williams, W. M. McGee, M. J. Ashwin, T. S. Jones, E. Clarke, P. Stavrinou, J. Zhang, S. Tomic, and C. P. A. Mulcahy, Appl. Phys. Lett. **90**, 032109 (2007).
[7] J. D. Perkins, A. Mascarenhas, Y. Zhang, J. F. Geisz, D. J. Friedman, J. M. Olson, and S. R. Kurtz, Phys. Rev. Lett. **82**, 3312 (1999).
[8] Y. Zhang, A. Mascarenhas, H. P. Xin, and C. W. Tu, Phys. Rev. B **61**, 7479 (2000).
[9] I.-H. Ho and G. B. Stringfellow, J. Cryst. Growth **178**, 1 (1997).
[10] K. Uesugi and I. Suemune, J. Cryst. Growth **189–190**, 490 (1998).
[11] S. B. Zhang and A. Zunger, Appl. Phys. Lett. **71**, 677 (1997).
[12] S. B. Zhang and S.-H. Wei, Phys. Rev. Lett. **86**, 1789 (2001).
[13] D. Sentosa, X.-H. Tang, S. J. Chua, and Z.-Y. Yin, Adv. Mater. Res. **31**, 77 (2008).
[14] W. K. Loke, S. F. Yoon, T. K. Ng, S. Z. Wang, and W. J. Fan, J. Vac. Sci. Technol. B **20**, 2091 (2002).
[15] S. Dhar, N. Halder, and A. Mondal, Thin Solid Films **515**, 4427 (2007).
[16] W. M. Chen, I. A. Buyanova, C. W. Tu, and H. Yonezu, Acta Phys. Pol. A **108**(4), 571 (2005).
[17] R. Intartaglia, T. Taliercio, P. Lefebvre, P. Valvin, T. Bretagnon, T. Guillet, B. Gil, U. Tisch, E. Finkman, J. Salzman, M.-A. Pinault, and E. Tournie, IEE Proc.: Optoelectron. **151**(5), 365 (2004).
[18] P. R. C. Kent and A. Zunger, Phys. Status Solidi B **228**, 253 (2001).
[19] M. Herrera, D. González, J. G. Lozano, R. García, M. Hopkinson, H. Y. Liu, M. Gutiérrez, and P. Navaretti, J. Appl. Phys. **98**, 023521 (2005).
[20] M. Herrera, D. González, R. García, M. Hopkinson, P. Navaretti, M. Gutiérrez, and H. Y. Liu, Thin Solid Films **483**, 185 (2005).
[21] A. V. Crewe, J. Wall, and J. Langmore, Science **168**, 1338 (1970).
[22] K. van Benthem, A. R. Lupini, M. P. Oxley, S. D. Findlay, L. J. Allen, and S. J. Pennycook, Ultramicroscopy **106**, 1062 (2006).
[23] P. D. Nellist and S. J. Pennycook, Science **274**, 413 (1996).
[24] P. M. Voyles, D. A. Muller, J. L. Grazul, P. H. Citrin, and H.-J. J. Gossmann, Nature (London) **416**, 826 (2002).
[25] M. Varela, S. D. Findlay, A. R. Lupini, H. M. Christen, A. Y. Borisevich, N. Dellby, O. L. Krivanek, P. D. Nellist, M. P. Oxley, L. J. Allen, and S. J. Pennycook, Phys. Rev. Lett. **92**, 095502 (2004).
[26] M. Takeguchi, M. R. McCartney, and D. J. Smith, Appl. Phys. Lett. **84**, 2103 (2004).
[27] S. J. Pennycook, B. Rafferty, and P. D. Nellist, Microsc. Microanal. **6**, 343 (2000).
[28] D. D. Perovic, C. J. Rossouw, and A. Howie, Ultramicroscopy **52**, 353 (1993).
[29] M. M. J. Treacy, J. M. Gibson, K. T. Short, and S. B. Rice, Ultramicroscopy **26**, 133 (1988).
[30] V. Grillo, E. Carlino, and F. Glas, Phys. Rev. B **77**, 054103 (2008).
[31] X. Wu, M. D. Robertson, J. A. Gupta, and J.-M. Baribeau, J. Phys.: Condens. Matter **20**, 075215 (2008).
[32] Y. P. Peng, P. D. Nellist, and S. J. Pennycook, J. Electron Microsc. **53**, 257 (2004).
[33] Z. H. Yu, P. E. Batson, and J. Silcox, Ultramicroscopy **96**, 275 (2003).
[34] D. O. Klenov and S. Stemmer, Ultramicroscopy **106**, 889 (2006).
[35] R. F. Egerton, *Electron Energy-Loss in the Electron Microscope*, 2nd ed. (Plenum, New York, 1996).
[36] D. D. Perovic, Inst. Phys. Conf. Ser. **119**, 67 (1991).
[37] R. F. Egerton, *Electron Energy-loss Spectroscopy in the Electron Microscope*, 2nd ed. (Springer, New York, 1996).
[38] R. F. Egerton, Rep. Prog. Phys. **72**, 016502 (2009).
[39] M. Haider, S. Uhlemann, and J. Zach, Ultramicroscopy **81**, 163 (2000).
[40] G. Kresse and J. Furthmüller, Phys. Rev. B **54**, 11169 (1996).
[41] G. Kresse and D. Joubert, Phys. Rev. B **59**, 1758 (1999).
[42] J. Pizarro, P. L. Galindo, E. Guerrero, A. Yáñez, M. P. Guerrero, A. Rosenauer, D. L. Sales, and S. I. Molina, Appl. Phys. Lett. **93**, 153107 (2008).
[43] K. Ishizuka, Ultramicroscopy **90**, 71 (2002).
[44] S. D. Findlay, M. P. Oxley, and C. J. Rossouw, Ultramicroscopy **96**, 65 (2003).
[45] A. M. Sanchez, P. L. Galindo, S. Kret, M. Falke, R. Beanland, and P. J. Goodhew, Microsc. Microanal. **12**, 285 (2006).
[46] X. Wu and J.-M. Baribeau, J. Appl. Phys. **105**, 043517 (2009).
[47] K. Du, K. von Hochmeister, and F. Phillipp, Ultramicroscopy **107**, 281 (2007).
[48] R. A. Herring, Ultramicroscopy **106**, 960 (2006).
[49] C. R. Hall, P. B. Hirsch, and G. R. Booker, Philos. Mag. **14**, 979 (1966).
[50] P. Krispin, V. Gambin, J. S. Harris, and K. H. Ploog, J. Appl. Phys. **93**, 6095 (2003).
[51] M. Reason, H. A. McKay, W. Ye, S. Hanson, R. S. Goldman, and V. Rotberg, Appl. Phys. Lett. **85**, 1692 (2004).
[52] P. R. Chalker, T. J. Bullough, M. Gass, S. Thomas, and T. B. Joyce, J. Phys.: Condens. Matter **16**, S3161 (2004).
[53] A. Carvalho, S. J. Barkerb, R. Jonesa, R. S. Williamsb, M. J. Ashwinb, R. C. Newmanb, P. N. Stavrinoub, G. Parryb, T. S. Jonesb, S. Öbergc, and P. R. Briddond, Physica B **401–402**, 339 (2007).
[54] T. D. Moustakas and R. J. Molnar, Mater. Res. Soc. Symp. Proc. **281**, 753 (1993).
[55] R. P. Vaudo, J. W. Cook, and J. F. Schetzina, J. Crystal Growth **138**, 40 (1994).
[56] E. Iliopoulos, A. Adikimenakisa, E. Dimakisa, K. Tsagarakia, G. Konstantinidisa, and A. Georgakilas, J. Cryst. Growth **278**, 426 (2005).
[57] M. H. Du, S. Limpijumnong, and S. B. Zhang, Phys. Rev. Lett. **97**, 075503 (2006).